Journal of Alloys and Compounds 644 (2015) 317–323

Contents lists available at ScienceDirect

Journal of Alloys and Compounds

journal homepage: www.elsevier.com/locate/jalcom

Controlled formation of $MoSe_2$ by MoN_x thin film as a diffusion barrier against Se during selenization annealing for CIGS solar cell

Chan-Wook Jeon [a], Taehoon Cheon [b,c], Hangil Kim [b], Min-Su Kwon [a], Soo-Hyun Kim [b,*]

[a] School of Chemical Engineering, Yeungnam University, Gyeongsangbuk-do 712-749, Republic of Korea
[b] School of Materials Science and Engineering, Yeungnam University, Gyeongsangbuk-do 712-749, Republic of Korea
[c] Center for Core Research Facilities, DaeguGyeongbuk Institute of Science & Technology, Daegu, Republic of Korea

ARTICLE INFO

Article history:
Received 28 February 2015
Received in revised form 14 April 2015
Accepted 18 April 2015
Available online 28 April 2015

Keywords:
Mo
MoN_x
Diffusion barrier
Selenization
CIGS solar cell

ABSTRACT

This study investigated the interfacial reactions and electrical properties of a Mo single layer and Mo/MoN_x/Mo multilayer during high temperature selenization annealing. The Mo single layer was converted easily to $MoSe_2$, which was 7 times thicker than the Mo layer consumed ~900 nm, by selenization at 460 °C for 10 min and the sheet resistance increased 8 fold compared to that of the as-deposited Mo film. On the other hand, in the Mo/MoN_x/Mo structure, transmission electron microscopy (TEM) showed that the $MoSe_2$ transformation was localized only in the top Mo layer and the bottom Mo layer was completely unaffected, even after selenization at 560 °C. The sheet resistance of the multilayer was relatively unchanged by selenization. This suggests that the MoN_x layer performed well as a diffusion barrier against Se and the thickness of $MoSe_2$ can be controlled precisely by adjusting the top Mo layer thickness. Furthermore, TEM and energy dispersive spectroscopy analysis showed that the selenized multilayer consisted of $MoSe_2$/Mo/MoN_x/Mo, in which the top Mo layer of 60 nm was not fully converted to $MoSe_2$ and 20 nm was left unreacted. The residual Mo interlayer located at the interface of $MoSe_2$ and MoN_x is believed to be beneficial for the ohmic contact of the selenized multilayer.

1. Introduction

Among thin film solar cells reported thus far, Cu(In, Ga)$(S, Se)_2$ (CIGS) solar cells have the highest conversion efficiency at 21.7% [1]. These small-area solar cells feature CIGS absorber layers prepared by a co-evaporation method. Recently, Solar Frontier announced a record conversion efficiency of 20.9% with CIGS produced based on sulfurization after selenization (SAS) [2]. This two-step process, which is comprised of metal precursor deposition followed by chalcogenization, is used widely in the production of large-area modules. Typically, a CIGS absorber layer is formed on top of a Mo back contact. The chalcogenization step of the two-step process involves selenization at relatively low temperatures followed by sulfurization at high temperatures. During the two-step process, the surface of the Mo back contact reacts with Se to form a $MoSe_2$ layer. While Mo selenide facilitates the ohmic contact of CIGS and Mo [3], it can cause a decrease in the fill factor arising from high series resistance [4] or delamination [5] when formed with an excessive thickness. The conversion efficiency increases at higher heat treatment temperatures due to the enhanced structural and electrical quality of CIGS [6], but this entails a trade-off with an excessively thick $MoSe_2$ layer in the case of the two-step process. Therefore, to utilize the benefits of working at high temperatures, it is essential to control the thickness of $MoSe_2$. According to Wada et al., the selenization of Mo is accelerated in the presence of Na [7] because the Se activity increases on the Mo surface in the form of Na polyselenide. Removing Na to suppress $MoSe_2$ growth, however, is not recommended Because Na is essential for creating high-efficiency CIGS solar cells. Another study showed that O in Mo thin films helps suppress the formation of Mo selenide [8]; however, O should not be used to remove $MoSe_2$ because it not only increases Mo resistivity but also suppresses Na diffusion [8].

In this study, the formation of $MoSe_2$ was controlled by introducing a Se diffusion barrier in the middle of the Mo layer. The diffusion barrier must ensure chemical stability with surrounding materials up to the follow-up heat treatment process and prevent the diffusion of some elements. In the manufacture of semiconductor devices, transition metals, such as Ta, Ti, W, and Mo, and their nitrides, such as TaN_x, TiN, WN_x, and MoN_x have been used as diffusion barriers [9,10]. Many investigations on applying such diffusion barriers to Cu show that transition metal nitrides are more effective in preventing diffusion at higher temperatures than transition metals [11–17]. The outstanding diffusion barrier

* Corresponding author.

http://dx.doi.org/10.1016/j.jallcom.2015.04.120
0925-8388/

performance of transition metal nitrides can be attributed to their excellent thermal stability, dense crystal structure of the interstitial compound, and the stuffing of grain boundaries by nitrogen during sputtering [18,19]. Although the characteristics of MoN_x as a diffusion barrier for Se have not been reported, the MoN_x layer and Mo/MoN_x bilayer are more effective in preventing Cu diffusion than a Mo layer [20]. Therefore, in this study, MoN_x was inserted as a diffusion barrier against Se in the Mo back contact layer to control the thickness of $MoSe_2$ formed during selenization annealing.

Most molybdenum nitride films have been deposited by physical vapor deposition (PVD), e.g., by sputtering [21–26] and ion beam-assisted deposition (IBAD) [27,28]. Chemical vapor deposition (CVD)-based methods are seldom used [29–31] and their use generally results in high resistivity and high levels of impurities within the films. This study deposited MoN_x films through reactive sputtering, which makes it possible to achieve more precise control of the compositions of the compound thin films by adjusting the flow rate of reactive gases and provides easier control of the physical properties. MoN_x forms ohmic contact with Mo and has a low resistivity, allowing the successful application of MoN/Mo to electrodes. Moreover, depending on the presence of reactive gases, processes involving Mo and MoN_x films can be carried out in the same vacuum chamber. This is expected to simplify the process and reduce the cost significantly. This study discussed the effects of MoN_x as a diffusion barrier for Se by analyzing the microstructure of thin-Mo and MoN_x layers after the selenization of a thin-Mo/MoN_x/thick-Mo multilayer at 460–560 °C under a Se vapor atmosphere.

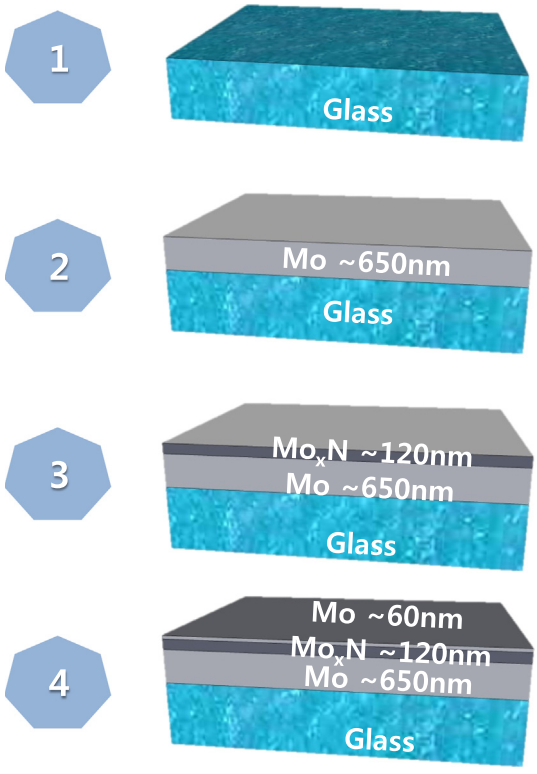

Fig. 1. Schematic diagram of sample structure.

2. Experimental

Mo and MoN_x thin films were deposited by RF (radio-frequency) magnetron sputtering with an N_2/Ar gas mixture. The Mo target used in the deposition process was 5 cm (2 in.) in diameter with a purity of 99.9999%. The flow rate of N_2 gas was varied and the characteristics of the MoN_x thin films were examined accordingly. As a substrate for Mo and MoN_x deposition, soda lime glass or thermally-grown SiO_2 (100 nm) covered Si wafer were used after RCA cleaning. During deposition, the temperature of the substrate and chamber was maintained at 150 °C, and the substrate was rotated at 3 revolutions per minute to allow uniform deposition. For all depositions, the initial vacuum was maintained at below 3.0×10^{-6} torr, and an RF power of 100 W was applied to the target. The flow rate of Ar gas was fixed to 20 sccm (standard cubic centimeter per minute), while that of the N_2 gas was varied from 2, to 14 sccm. The throttle valve was adjusted to maintain a pressure of 8 m torr throughout the deposition process.

Grazing-incidence angle (incident angle, $\theta = 3°$) X-ray diffraction (GIAXRD, PANalytical X'-pert MRD with Cu Kα radiation at 1.2 kW) was performed for phase and crystallinity identification. The resistivity was determined by combining the sheet resistance of the film measured using a four-point probe and the measured thickness. The composition and impurities were identified by Rutherford backscattering spectrometry (RBS). The nitrogen resonance RBS technique (incident energy of He^{++}: 3.695 MeV) was used to detect N in the film.

As shown in Fig. 1, a Mo layer of 650 nm was first deposited on top of the soda lime glass, followed by a 120 nm MoN_x layer, depending on the experimental conditions determined by the N_2 flow rate. A Mo thin film with a thickness of 60 nm was finally deposited. The effectiveness of the diffusion barriers for Se was assessed by comparing the Mo layer (~650 nm) and the $Mo/MoN_x/Mo$ multilayer (total thickness: ~830 nm) after selenization at 460 °C and 560 °C. Selenization was carried out by incorporating Se vapor in the rapid thermal process for ten minutes. The characteristics of the diffusion barriers were evaluated based on interfacial reaction analysis of the bright-field images, scanning TEM-high angle annular dark field (STEM-HAADF) analysis (Hitachi, HF-3300 equipped with 300 kV accelerating voltage and field emission gun) and energy dispersive spectroscopy (EDS). The TEM images were taken digitally using a 2 k × 2 k (2048 pixel × 2048 pixel) charge coupled device (CCD) camera (Gatan UltraScan™ 2000).

3. Results and discussion

Fig. 2 shows the change in resistivity with increasing N_2 flow rate. The Mo thin film deposited using Ar plasma without N_2 had a resistivity of 24 μΩ-cm. When 2 sccm of N_2 gas was flowed into the chamber, the resistivity of the thin film increased to

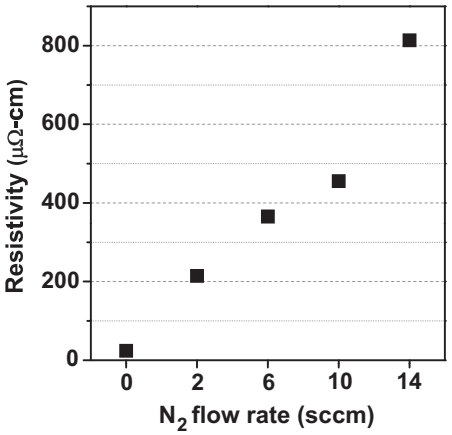

Fig. 2. Resistivity of the films as a function of N_2 flow rate.

214 μΩ-cm. Overall, the resistivity of the deposited film increased with increasing N_2 flow rate. When the flow rate of N_2 gas in the chamber was increased to 14 sccm, the resistivity was ~813 μΩ-cm. This is because the electrical resistance increases with the formation of molybdenum nitride from the metal Mo due to the incorporation of N in the thin film at higher N_2 flow rates.

Fig. 3 shows the XRD patterns of the deposited films at different N_2 flow rates. Under all deposition conditions, the largest peak was observed at 40.5° 2θ, which was assigned to the (1 1 0) plane of Mo with a body centered cubic (BCC) crystal structure. The (1 1 0) peak of the Mo thin film indicates a crystal structure suitable for growth into the (1 1 2) surface of the CIGS thin films. When the N_2 flow rate was increased to 2 sccm, the XRD pattern of the molybdenum nitrides could not be observed. This suggests that the crystal structure is maintained despite the small amounts of N in Mo. On the

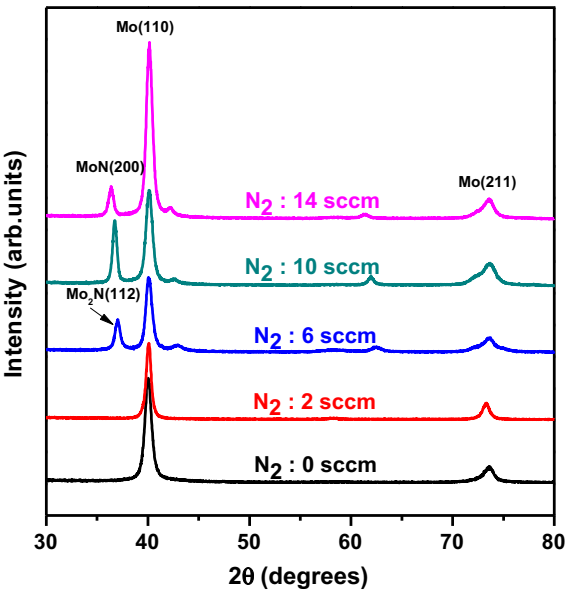

Fig. 3. XRD results of the films as a function of N_2 flow rate.

other hand, a Mo_2N phase formed when the N_2 flow rate was increased to 6 sccm because an increase in the amount of reactive gas leads to greater incorporation of N into the film. When the flow rate of the reactive gas N_2 was increased to 10 sccm, the intensity of the XRD peak (1 1 2) of Mo_2N increased. When the N_2 flow rate was increased further to 14 sccm, the formation of a MoN phase, which is richer in N compared to Mo_2N, is observed.

Rutherford Backscattering Spectrometry (RBS) was performed to understand phase formation as a function of the N_2 gas flow rate. A resonance RBS technique using He^{++} with an incident energy of 3.695 MeV as well as conventional RBS using He^{++} with an incident energy of 2 MeV was used to sensitively detect the low-mass element in the film, such as nitrogen. No backscattering peak from N was detected when the incident energy of He^{++} was 2 MeV (data not shown). This was attributed to the low scattering cross sections of N. Therefore, the backscattering signals from N are buried in the backscattering signals from the higher-mass substrate, SiO_2. On the other hand, when the incident He^{++} energy was 3.695 MeV, as shown in Fig. 4, the scattering cross-section did not follow a normal Rutherford one and was significantly higher than that of normal Rutherford scattering, which is called resonance RBS. The backscattering signals from N in the MoN_x film could be observed clearly using N resonance RBS. Fig. 4(a) presents

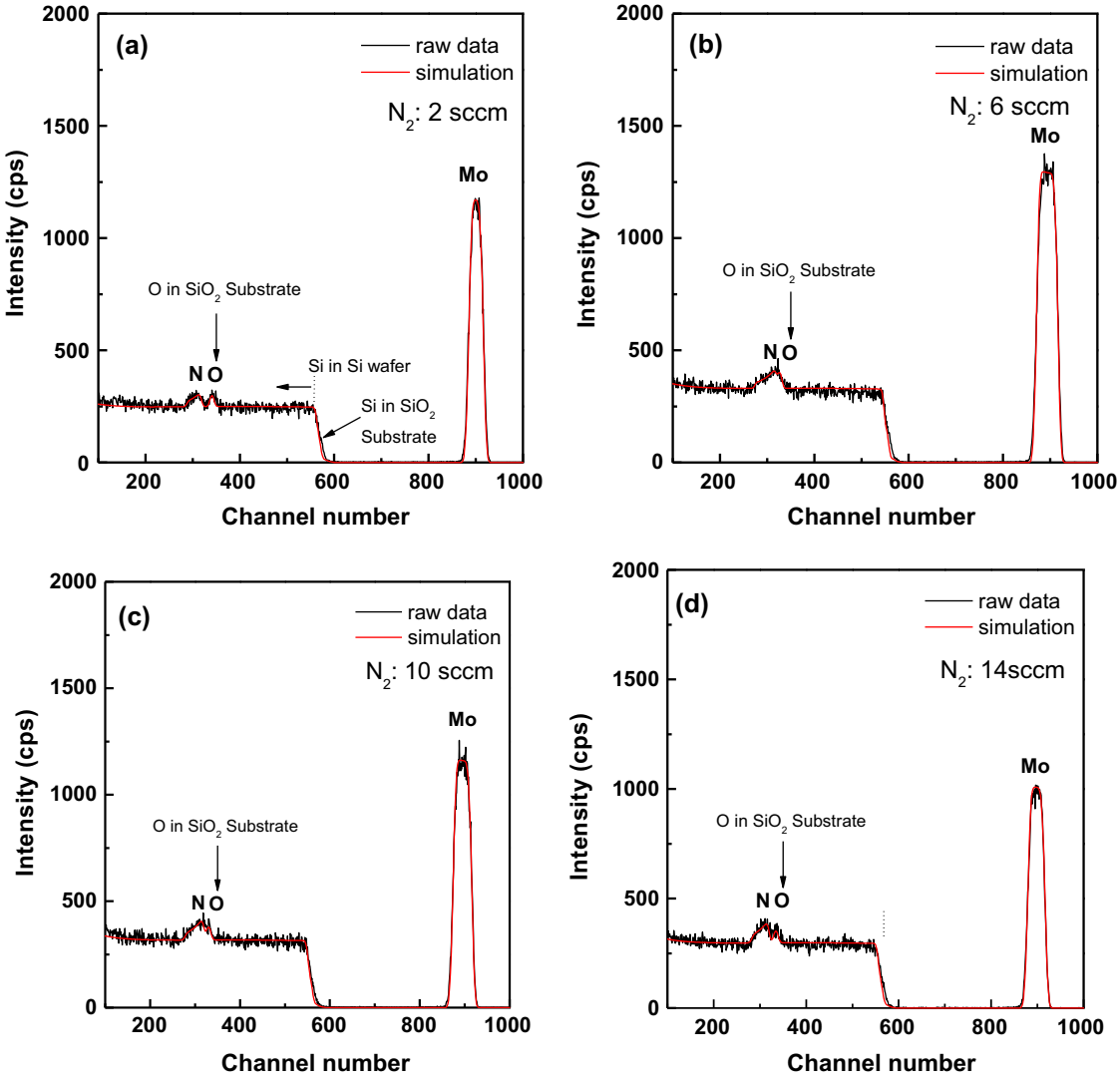

Fig. 4. Nitrogen resonance RBS results as a function of N_2 flow rate; (a) N_2: 2 sccm, (b) N_2: 6 sccm, (c) N_2: 10 sccm, and (d) N_2: 14 sccm.

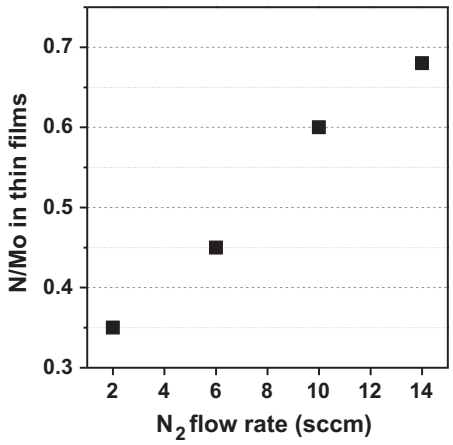

Fig. 5. Atomic ratio of N/Mo in thin films as a function of N_2 flow rate. The results were obtained from RUMP simulation based on nitrogen resonance RBS results shown in Fig. 4.

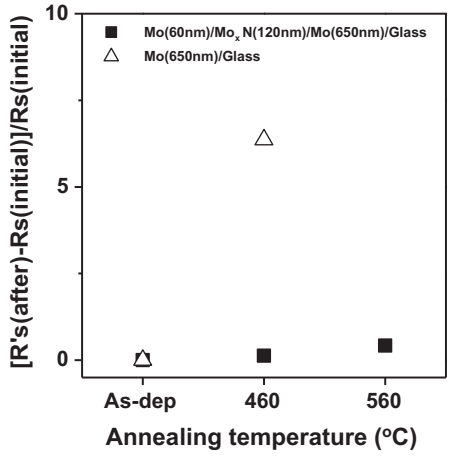

Fig. 6. Sheet resistance change after selenization annealing with sample structures.

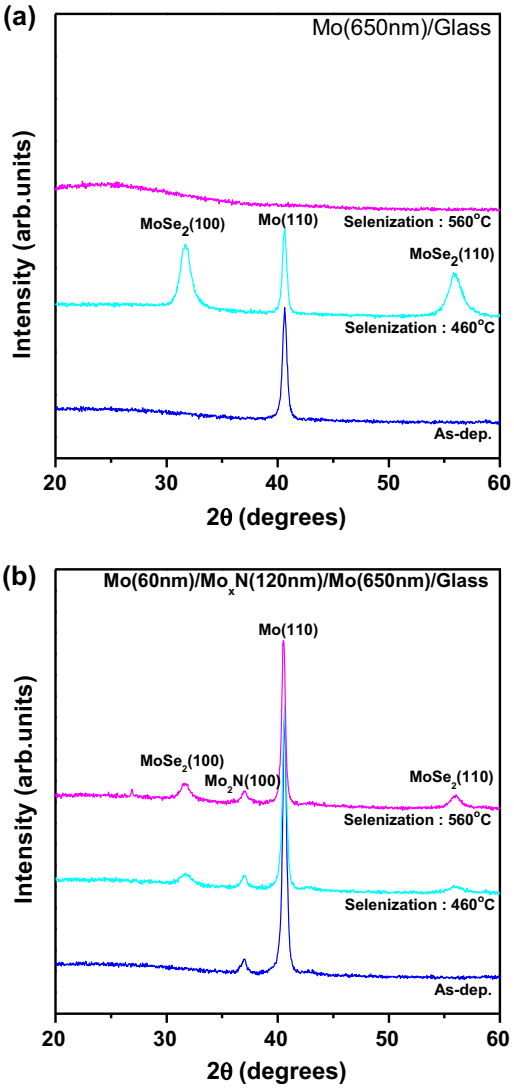

Fig. 7. (a) XRD results with selenization annealing for Mo (650 nm)/glass and (b) Mo (60 nm)/Mo_xN (120 nm)/Mo (650 nm)/glass.

the results of N resonance RBS analysis of a film deposited at a N_2 gas flow rate of 2 sccm. The heavy Mo was detected in the high channels (backscattered He^{++} with a relatively higher energy), whereas the lighter N was observed in the low channels (backscattered He^{++} with a relatively lower energy). The amount of carbon impurities within the film was 2 at.%, which can be attributed to chamber contamination. At a slightly higher channel than the channel in which N was detected, O was observed as signals of the SiO_2 substrate (100 nm in thickness). As the flow rate of the reactive gas was increased (Fig. 4(b)–(d)), the intensity of backscattered He^{++} from collisions with N increases, indicating an increase in the amount of N within the film.

Quantitative analysis of the film composition was obtained through a RUMP simulation of the nitrogen resonance RBS results. Fig. 5 shows the atomic ratio of N/Mo according to the deposition conditions. As shown in the Fig. 5, the ratio of N/Mo in the films increased with increasing N_2 flow rate in the plasma gas. When 2 sccm N_2 was added, the N/Mo ratio of the deposited film was 0.35. When the flow rate was 14 sccm, the ratio increased to 0.68. According to Jehn and Ettmaye [32], when the atomic ratio of N/Mo is less than 0.40, the main phase is Mo. With increasing nitrogen content ranging from an atomic ratio of 0.40 to 0.54, the main phase was Mo_2N, including β-Mo_2N and γ-Mo_2N. β-Mo_2N will transform to the γ-Mo_2N phase with higher temperature annealing and a higher nitrogen content. The nitrogen content ranged from 0.54 to 0.67; the main phase was Mo_3N_2. Furthermore, molybdenum nitride with nitrogen content higher than 0.67 has a main phase of MoN [33]. These results mostly coincide with the XRD results in Fig. 3 and RBS results in Fig. 5. From Figs. 3 and 5, a Mo_2N thin film with an N/Mo ratio of 0.46 was obtained at an N_2 flow rate of 6 sccm. When the N_2 flow rate was increased to 14 sccm, a MoN film with a N/Mo ratio of 0.68 was produced. These results show that thin films of different phases and various compositions such as Mo, Mo_2N and MoN, can be obtained by varying the N_2 flow rate and adjusting the amount of incorporated nitrogen.

The performance of MoN_x diffusion barriers against Se were characterized after selenization annealing of both a multilayer structure with MoN_x,(Mo/MoN_x/Mo) and Mo single layer. Fig. 6 shows the change in sheet resistance after selenization annealing of the multilayer with a MoN_x diffusion barrier deposited at a N_2 flow rate of 10 sccm. As shown in the figure, the sheet resistance of the Mo thin film increased 8 fold after selenization at 460 °C for 10 min. After selenization at 560 °C, it was impossible to measure the sheet resistance due to the delamination of the thin film with the thick formation of $MoSe_2$. For the Mo/MoN_x/Mo

multilayer, however, the sheet resistance did not change significantly even after selenization at 560 °C, indicating that the Mo/MoN_x/Mo structure remained stable.

XRD analysis was performed to evaluate the structural stability of the samples after selenization annealing. Fig. 7(a) shows the XRD patterns after selenization for 10 min at 460 °C and at 560 °C for a Mo single layer. XRD results showed crystalline $MoSe_2$ formed after selenization annealing the Mo single layer at 460 °C. But, as mentioned earlier, the sample subjected to selenization at 560 °C for 10 min exhibited an amorphous substrate peak due only to delamination of the film. The sample subjected to selenization at 460 °C for 10 min showed a decrease in the Mo (1 1 0) peak, and displayed two peaks corresponding to the (1 0 0) and (1 1 1) planes of the $MoSe_2$ phase. These peaks were observed when the $MoSe_2$ phase grew in the *c*-axis direction [34]. Therefore, XRD showed that in case of a Mo single layer, after selenization at 460 °C, most of the Mo layer experienced a phase transformation to the $MoSe_2$ phase due to Se diffusion. As shown in Fig. 7(b), however, the intensity of the Mo (1 1 0) peak of the Mo/MoN_x/Mo multilayer structure remained similar after selenization at 460 °C and 560 °C, and the Mo_2N (1 1 0) peak was clearly visible. The XRD peak from the $MoSe_2$ phase had weaker intensity compared to the case without MoN_x, and no significant changes were observed even with increasing selenization temperature. These results suggest that although the thin Mo layer in the upper part of the Mo/MoN_x/Mo multilayer had transformed to $MoSe_2$ during selenization, the lower thick Mo layer was protected from selenization by the MoN_x layer preventing Se diffusion into the lower Mo.

Cross-section TEM (XTEM) analysis was carried out for a closer examination of the interfacial reactions and the diffusion behavior of Se after selenization annealing. Fig. 8(a) and (b) shows the structural stability of the Mo single layer sample after selenization. From Fig. 8(a), a Mo thin film with a columnar grain structure was deposited successfully on the substrate. After selenization annealing of this Mo single layer at 460 °C for 10 min, (Fig. 8(b)), a very thick (~950 nm) $MoSe_2$ layer formed rapidly, and the resulting $MoSe_2$ had a thickness that was 7 times that of the consumed Mo ($T_{\Delta Mo}$) ($T_{MoSe2}/T_{\Delta Mo}$ = ~7). From the XTEM image of the Mo/MoN_x/Mo structure before selenization, the thick Mo and MoN_x were deposited as the lower layers and a thin Mo layer was deposited as the top layer on the glass wafer (Fig. 8(c)). After selenization at 460 °C for 10 min, the sample with the Mo/MoN_x/Mo structure formed $MoSe_2$ with a thickness of ~150 nm, as shown in Fig. 8(d), which was significantly lower than that of the Mo single layer, and the lower MoN_x/Mo layer remained stable. As shown in Fig. 8(e), the MoN_x/Mo structure remained stable even after selenization at 560 °C, and the only difference was that the thickness of $MoSe_2$ increased slightly to ~180 nm. Here, the upper thin Mo layer did not transform fully to $MoSe_2$ and remained between $MoSe_2$ and MoN_x at a thickness of 20–30 nm. Interestingly, the thickness of $MoSe_2$ formed was four times that of consumed Mo ($T_{MoSe2}/T_{\Delta Mo}$ = ~4), which was far lower than that in the single layer Mo structure. This suggests that the Mo deposited on the MoN_x phase has greater resistance to selenization, and the resulting $MoSe_2$ has a higher density. This residual Mo is expected to play a positive role in reducing the contact resistance of $MoSe_2$/MoNx.

To characterize the interfacial reaction, the Se diffusion behavior and structural stability, STEM-HAADF (High angle annular dark field) analysis and EDS mapping were conducted for both the Mo single layer and multilayered samples after selenization annealing at 460 °C. Fig. 9(a) shows the STEM-HAADF image of the sample with a Mo single layer after selenization annealing at 460 °C. Mo and $MoSe_2$ could be distinguished clearly due to the difference in atomic weight. EDS showed that Se was distributed uniformly throughout the entire $MoSe_2$ formed (Fig. 9(b) and (c)). Fig. 10(a)

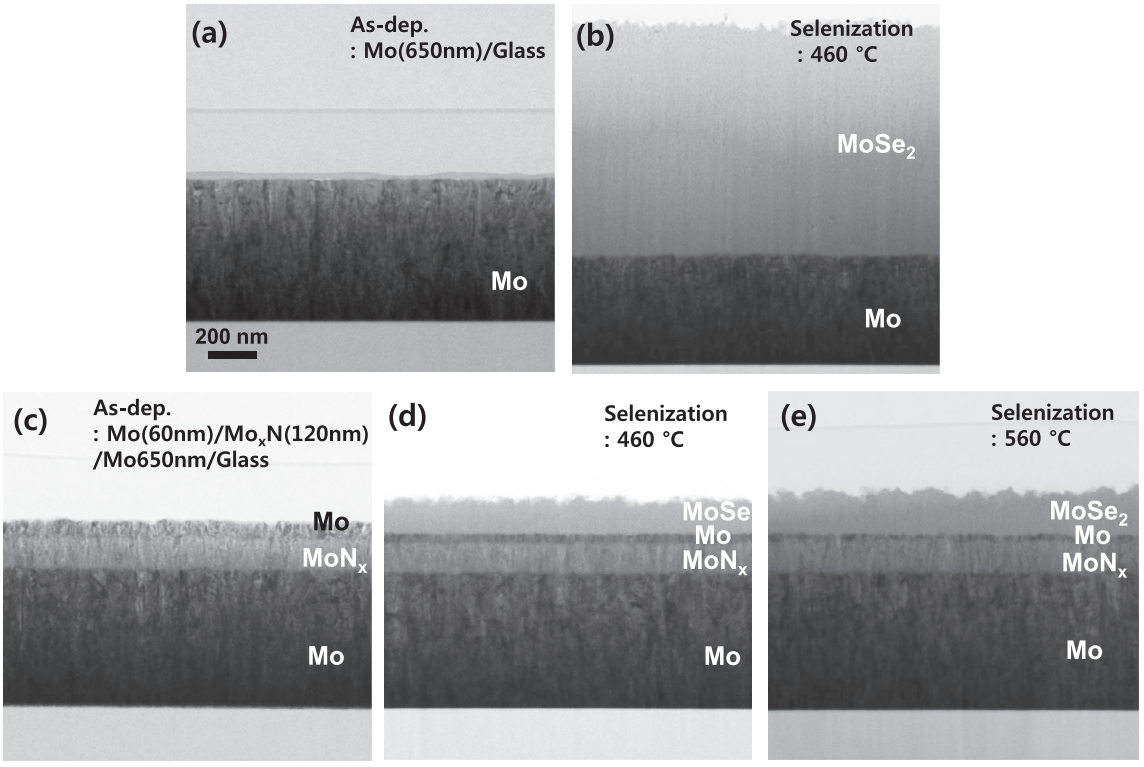

Fig. 8. XTEM analysis results; (a) Mo (650 nm)/glass, (as-dep.), and (b) Mo (650 nm)/glass, (460 °C selenazation.), (c) Mo (60 nm)/Mo_xN (120 nm)/Mo (650 nm)/glass, (as-dep.), (d) Mo (60 nm)/Mo_xN (120 nm)/Mo (650 nm)/glass, (460 °C selenazation), and (e) Mo(60 nm)/Mo_xN(120 nm)/Mo (650 nm)/glass, (560 °C selenazation).

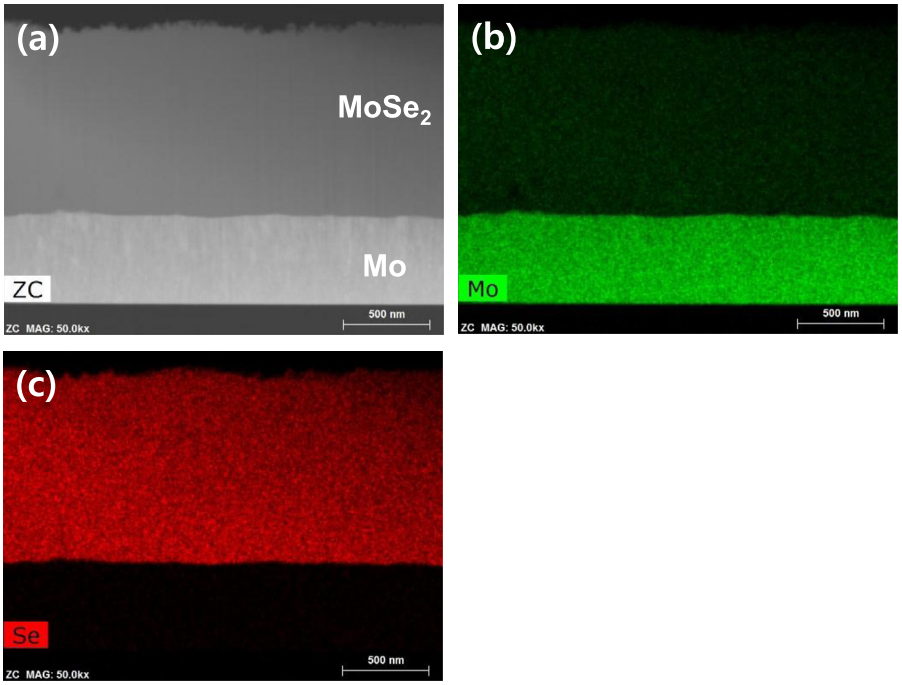

Fig. 9. (a) STEM-HAADF image analysis of the sample Mo (650 nm)/glass after selenization annealing at 460 °C, (b) corresponding EDS elemental mapping for Mo, and (c) Se.

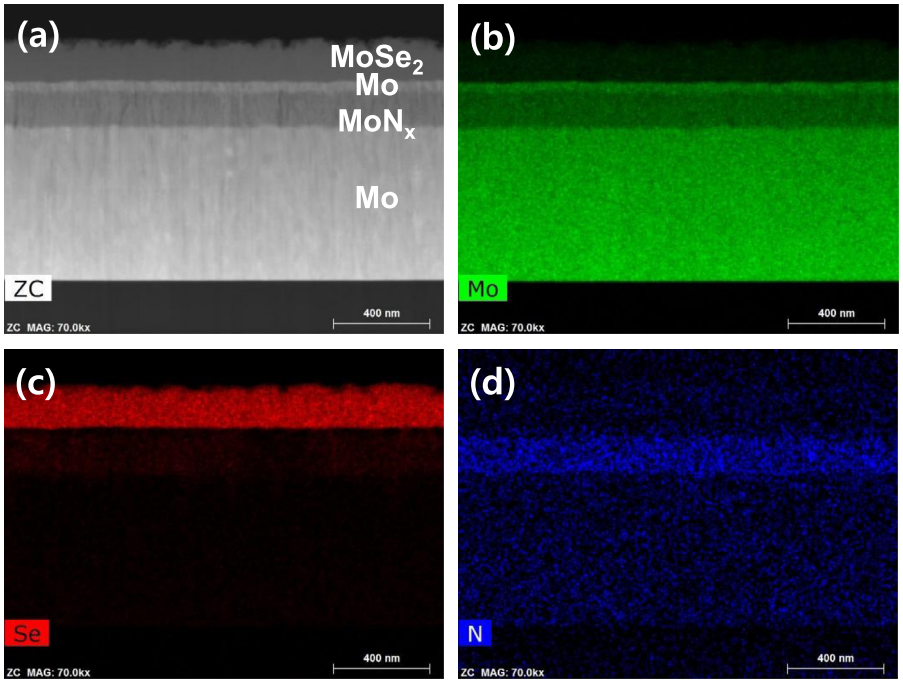

Fig. 10. (a) STEM-HAADF image analysis of the sample Mo (60 nm)/Mo_xN (120 nm)/Mo (650 nm)/glass after selenization annealing at 460 °C, (b) corresponding EDS elemental mapping for Mo, (c) Se, and (d) N.

presents a STEM-HAADF image of the Mo/MoN_x/Mo multilayered sample after selenization annealing at 460 °C. As observed in the TEM bright-field image (Fig. 8(d)), the thick Mo layer deposited on the glass wafer was prevented from the selenization, and only a part of the upper thin Mo transformed to $MoSe_2$. The difference in atomic mass was visible in the remaining Mo and MoN_x films. From EDS mapping, the interfaces of the $MoSe_2$/Mo/MoN_x/Mo structure were compositionally abrupt (Figs. 10(b)–(d)), and MoN_x effectively prevented Se diffusion into the thick lower Mo (Fig. 10(c)). After selenization, the nitrogen signals were only present in MoN_x, which suggests that the deposited MoN_x is thermally stable and is maintained without decomposition. Overall, the MoN_x

layer inserted between the Mo layers exhibits outstanding diffusion barrier performance, effectively suppressing the diffusion of Se, even after selenization at 460 °C.

4. Conclusions

This study proposed a Mo/MoN_x/Mo multilayer to suppress the excessive formation of $MoSe_2$, as a result of selenization annealing, which was identified as a problem of using Mo as electrodes in solar cells. Based on XRD analysis and nitrogen resonance RBS analysis, the amount of nitrogen incorporated into the Mo film could be controlled precisely by the N_2 flow rate. Through this process, thin films of different phases and various compositions, such as Mo, Mo_2N, and MoN, could be obtained. The Mo/MoN_x/Mo multilayer was deposited successfully in the same chamber where Mo deposition took place. Through XRD and STEM-EDS analyses, the MoN_x film effectively prevented Se diffusion compared to Mo, making it possible to control the thickness of $MoSe_2$ formed after selenization annealing. Furthermore, TEM analysis showed that the final structure of the multilayered sample after selenization annealing was not a simple $MoSe_2$/MoN_x/Mo one, but a $MoSe_2$/Mo/MoN_x/Mo one consisting of a thin Mo layer (10–20 nm) located on the $MoSe_2$/MoN_x interface. As the $MoSe_2$/Mo, Mo/MoN_x and MoN_x/Mo interfaces show ohmic contact behavior, the proposed scheme eliminates the possibility of the formation of Schottky contact. Therefore, the self-formation of ohmic contacts during CIGS manufacturing provide an additional advantage of the proposed scheme instead of preventing the excessive formation of $MoSe_2$ through the introduction of a MoN_x diffusion barrier. Therefore, the proposed scheme is expected to have a positive impact when applied to the manufacture of CIGS solar cells.

Acknowledgements

This work was supported by the New & Renewable Energy of the Korea Institute of Energy Technology Evaluation and Planning (KETEP) grant funded by the Korean government Ministry of Knowledge Economy (No. 20123010010130), by the Ministry of Trade, Industry & Energy (MOTIE), Korea Institute for Advancement of Technology(KIAT) and DaeGyeong Institute for Regional Program Evaluation (DGIRPE) through the Leading Industry Development for Economic Region (R0002227), and by Korea Research Foundation (NRF-2012H1B8A2025602).

.

References

[1] P. Jackson, D. Hariskos, R. Wuerz, O. Kiowski, A. Bauer, T.M. Friedlmeier, M. Powalla, Phys. Status Solidi Rapid Res. Lett. 9 (2015) 28–31.
[2] Martin A. Green, Keith Emery, Yoshihiro Hishikawa, Wilhelm Warta, Ewan D. Dunlop, Prog. Photovolt.: Res. Appl. 22 (2014) 701–710.
[3] T. Sakurai, M.M. Islam, H. Uehigashi, S. Ishizuka, A. Yamada, K. Matsubara, S. Niki, K. Akimoto, Solar Energy Mater. Solar Cells 95 (2011) 227–230.
[4] Xiaolong Zhu, Zhen Zhou, Yaoming Wang, Lei Zhang, Aimin Li, Fuqiang Huang, Solar Energy Mater. Solar Cells 101 (2012) 57–61.
[5] SeJin Ahn, Ki Hyun Kim, Jae Ho Yun, Kyung Hoon Yoon, J. Appl. Phys. 105 (2009) 113533.
[6] Li Zhang, Qing He, Wei.-Long Jiang, Fang.-Fang Liu, Chang.-Jian. Li, Yun Sun, Solar Energy Mater. Solar Cells 93 (2009) 114–118.
[7] T. Wada, N. Kohara, S. Nishiwaki, T. Negami, Thin Solid Films 387 (2001) 118–122.
[8] J. Palm, V. Probst, A. Brummer, W. Stetter, R. Tolle, T.P. Niesen, S. Visbeck, O. Hernandez, M. Wendl, H. Vogt, H. Calwer, B. Freienstein, F. Karg, Thin Solid Films 431–432 (2003) 514–522.
[9] S.-Q. Wang, Mater. Res. Bull. 19 (8) (1994) 30.
[10] A.E. Kaloyeros, E.T. Eisenbraun, Annu. Rev. Mater. Sci. 30 (2000) 363–385.
[11] S.-Q. Wang, I. Raaijmakers, B.J. Burrow, S. Suthar, S. Redkar, K.-B. Kim, J. Appl. Phys. 68 (1990) 5176.
[12] K.-C. Park, K.-B. Kim, J. Electrochem. Soc. 142 (1995) 3109.
[13] K. Holloway, P.M. Fryer, C. Cabral Jr., J.M.E. Harper, P.J. Bailey, K.H. Kelleher, J. Appl. Phys. 71 (1992) 5433.
[14] T. Oku, E. Kawakami, M. Uekubo, K. Takahiro, S. Yamaguchi, M. Murakami, Appl. Surf. Sci. 99 (1996) 265.
[15] M. Takeyama, A. Noya, T. Sase, A. Ohta, K. Sasaki, J. Vac. Sci. Tech. B 14 (1996) 674.
[16] B.-S. Suh, Y.-J. Lee, J.-S. Hwang, C.-O. Park, Thin Solid Films 348 (1999) 299.
[17] H.P. Kattelus, E. Kolawa, K. Affolter, M.-A. Nicolet, J. Vac. Sci. Tech. A3 (1985) 2246.
[18] H.P. Kattelus, M.-A. Nicolet, Deevendra Gupa, Paul S. Ho, Noyes Publications, Park Ridge, New Jersey, US, 1998, p. 432.
[19] K.-M. Chang, T.-H. Yeh, I.-C. Deng, J. Appl. Phys. 81 (1997) 3670–3676.
[20] S. Song, Y. Liu, D. Mao, H. Ling, M. Li, Thin Solid Films 476 (2005) 142–147.
[21] R. Sanjinés, P. Hones, F. Lévy, Thin Solid Films 332 (1998) 225–229.
[22] P. Hones, N. Martin, M. Regula, F. Lévy, J. Phys. D Appl. Phys. 36 (2003) 1023–1029.
[23] J.-Y. Lee, J.-W. Park, Jpn. J. Appl. Phys. 35 (1996) 4280–4284.
[24] J.-C. Chuang, S.-L. Tu, M.-C. Chen, Thin Solid Films 346 (1999) 299–306.
[25] Y. He, J.Y. Feng, J. Cryst. Growth 263 (2004) 203–207.
[26] V.P. Anitha, S. Major, D. Chandrashekharam, M. Bhatnagar, Surf. Coat. Tech. 79 (1996) 50–54.
[27] H.J. Lee, J.-G. Choi, C.W. Colling, M.S. Mudholkar, L.T. Thompson, Appl. Surf. Sci. 89 (1995) 121–130.
[28] M.S. Mudholkar, L.T. Thompson, J. Appl. Phys. 77 (1995) 5138–5143.
[29] S.L. Roberson, D. Finello, R.F. Davis, Thin Solid Films 324 (1998) 30–36.
[30] M. Juppo, M. Ritala, M. Leskelä, J. Electrochem. Soc. 147 (2000) 3377–3381.
[31] R.M. Fix, R.G. Gordon, D.M. Hoffman, J. Am. Chem. Soc. 112 (1990) 7833–7835.
[32] H. Jehn, P. Ettmayer, J. Less-Common Met. 58 (1978) 85.
[33] B.-Y. Tsui, C.-F. Huang, C.-H. Lu, J. Electrochem. Soc. 153 (3) (2006) G197–G202.
[34] D. Abou-Ras, G. Kostorz, D. Bremaud, M.M. Kälin, F.V. Kurdesau, A.N. Tiwari, M. Döbeli, Thin Solid Films 480–481 (2005) 433–438.